Anomalies in the gravitational recoil of eccentric black-hole mergers with unequal mass ratios

Miren Radia,[1,*] Ulrich Sperhake,[1,2,†] Emanuele Berti,[3,‡] and Robin Croft[1]

[1]*Department of Applied Mathematics and Theoretical Physics, Centre for Mathematical Sciences, University of Cambridge, Wilberforce Road, Cambridge CB3 0WA, United Kingdom*
[2]*California Institute of Technology, Pasadena, California 91125, USA*
[3]*Department of Physics and Astronomy, Johns Hopkins University, 3400 N. Charles Street, Baltimore, Maryland 21218, USA*

(Received 28 January 2021; accepted 18 March 2021; published 6 May 2021)

The radiation of linear momentum imparts a recoil (or "kick") to the center of mass of a merging black-hole binary system. Recent numerical relativity calculations have shown that eccentricity can lead to an approximate 25% increase in recoil velocities for equal-mass, spinning binaries with spins lying in the orbital plane ("superkick" configurations) [U. Sperhake *et al.* Phys. Rev. D **101**, 024044 (2020)]. Here we investigate the impact of nonzero eccentricity on the kick magnitude and gravitational-wave emission of nonspinning, unequal-mass black hole binaries. We confirm that nonzero eccentricities at merger can lead to kicks which are larger by up to ∼25% relative to the quasicircular case. We also find that the kick velocity v has an oscillatory dependence on eccentricity, which we interpret as a consequence of changes in the angle between the infall direction at merger and the apoapsis (or periapsis) direction.

DOI: 10.1103/PhysRevD.103.104006

I. INTRODUCTION

Gravitational waves (GWs) carry energy, angular momentum, and linear momentum away from the source with potentially observable consequences. The radiated energy corresponds to an often enormous mass deficit in the source; for example, the first ever detected black-hole (BH) binary merger, GW150914 [1], radiated $\Delta M \approx 3\ M_\odot$, or about 4.6% of the total mass of the source. A tiny fraction of this energy is deposited into GW interferometers, thus enabling us to detect and characterize the signal [2]. The angular momentum radiated in GWs reduces the rotation rate of possible merger remnants and—at least in four spacetime dimensions—plays a critical role in avoiding the formation of naked singularities in the form of BHs spinning above the Kerr limit; see, e.g., Refs. [3,4]. Therefore, GW emission is a necessary ingredient of the theory of general relativity, in the sense that it avoids the formation of spacetime singularities and preserves its predictive power.

In this paper, we focus on the radiated linear momentum, which imparts a recoil (commonly referred to as a *kick*) on the center of mass of the emitting system [5–7].

Whereas GWs inevitably carry energy and angular momentum—provided their sources do—the radiation of linear momentum requires some degree of asymmetry, as realized in nonspherical supernova explosions or unequal-mass ratios and/or spin misalignments in binary BH mergers. The inspiral of two equal-mass, nonspinning BHs, for example, radiates energy and angular momentum, whereas the emitted linear momentum is zero by symmetry. By turning these considerations around, we may also regard the study of recoiling GW emitters as a guided search for characteristic (in some loose sense "asymmetric") features in their orbital dynamics which, in turn, might help us to better understand astrophysical sources through GW observations. A recoiling postmerger BH, for example, can induce a blue (or red) shift in parts of its GW signal that may be exploited in future GW observations to directly measure BH kicks [8–10], and the effect of kicks should be taken into account in future ringdown tests of general relativity with third-generation GW detectors to avoid systematic biases [11]. The asymmetric emission of GWs is not the only mechanism that can contribute to recoils; if there is an accretion disk or some other astrophysical background, this can also impart a kick on the remnant BH that can be $\mathcal{O}(100)$ km/s [12].

For binary BH mergers, early estimates of the recoil speeds of the remnant BH relied on a variety of approximations, including post-Newtonian (PN) theory [13,14], BH perturbation theory [15], the effective-one-body formalism [16], the close-limit approximation [17,18], and combinations thereof [19]. Not long afterwards, during the numerical relativity (NR) gold rush, several groups obtained more accurate results for the kick velocity from the merger of nonspinning BHs along quasicircular orbits [20–22]. These calculations were

*m.r.radia@damtp.cam.ac.uk
†u.sperhake@damtp.cam.ac.uk
‡berti@jhu.edu

followed by the discovery that the merger of spinning BHs can lead to kick velocities of ~3000 km/s when the spins lie in the orbital plane and point in opposite directions ("superkick" configurations [23–25]), and to even larger kicks of order ~5000 km/s when the spins are partially aligned with the orbital angular momentum ("hang-up kick" configurations [26]). The probability of such large recoils occurring in nature depends therefore on spin alignment, and this has been studied by several authors (see, e.g., Refs. [27–31]).

The possible occurrence of superkicks has important consequences for astrophysical BHs and their environments [32–35]. It is pertinent to compare the recoil velocities obtained from NR simulations with the escape velocities of various astrophysical environments [36]. For example, stellar-mass BH binaries are believed to form dynamically in globular clusters [37]. In this case, the escape velocities are generally $\mathcal{O}(10)$ km/s, smaller than the $\mathcal{O}(100)$ km/s kicks predicted for quasicircular, nonspinning binaries [21]. Then, relativistic recoils can affect the proportion of BH merger remnants that are retained by globular clusters even if the BHs are nonspinning [38]. At the other end of the scale, the recoil velocities of supermassive BHs can be used to constrain theories of their growth at the center of dark matter halos [39]. Kicked remnants in the accretion disk of an active galactic nucleus may also lead to detectable electromagnetic counterparts for stellar-origin BH mergers [40,41].

As mentioned above, a net gravitational recoil requires some asymmetry in the system, so that the GW emission is anisotropic. A natural way to accentuate the asymmetry is through the addition of orbital eccentricity. Early calculations in the close-limit approximation [18] predicted a kick proportional to $1 + e$ for small eccentricities, $e \lesssim 0.1$. More recently, numerical relativity calculations led to the conclusion that eccentricity can lead to an approximate 25% increase in recoil velocities for superkick configurations with moderate eccentricities [42].

The main goal of this study is to investigate the impact of nonzero eccentricity on the kick magnitude and the corresponding GW emission of nonspinning, unequal-mass BH binaries. As we shall see, the eccentricity has a subtle but significant effect on the kick magnitude, which manifests itself in corresponding patterns in the GW signal, especially in subdominant multipoles.

For isolated binary systems with large initial separations, the emission of GWs acts to circularize the orbit by the time the signal enters the frequency band of ground-based detectors. However, viable dynamical formation channels of stellar-origin BH binaries could result in a non-negligible population of merging BHs that still retain moderate eccentricities at frequencies relevant for ground-based GW detection (see, e.g., Refs. [43–48]). Furthermore, the presence of astrophysical media such as accretion disks may increase the eccentricity during the inspiral [49]. Most of the events observed by the LIGO/Virgo Collaboration show no evidence of significant eccentricities [50], but the extraordinary GW190521 event [51] is potentially consistent with an eccentricity as high as $e \approx 0.7$ [52,53].

Orbital eccentricity is expected to be a distinguishing feature of stellar-origin BH binaries that form dynamically, but a nonzero eccentricity is more likely at the low frequencies accessible by LISA, where gravitational radiation reaction has less time to circularize the binary [54–56]. If confirmed, a nonzero eccentricity would hint at a possible dynamical origin for this event [52].

Eccentricity is expected to play an even more prominent role for massive BH binaries: the dynamics of these binaries in stellar and gaseous environments is expected to lead to distinct (but generically nonzero) orbital eccentricities by the time the binaries enter the LISA sensitivity window (see Ref. [57] and references therein). Even larger eccentricities are possible if BH binary coalescence occurs through the interaction with a third BH [58].

Our work is an exploration of the effect of large eccentricities near merger, and it differs in several ways from the catalog of eccentric, unequal-mass simulations presented in Ref. [59]. While their study considered a larger range of mass ratios (in our notation, $1/10 \leq q \leq 1$), they carried out fewer simulations for each value of q. The binaries in their simulations have initial eccentricities smaller than $e_0 = 0.18$ 15 cycles before merger, and since they start at larger orbital separations, their eccentricity will have further decreased by the time of merger. As we will see below, the larger initial eccentricities in our simulations allow us to highlight interesting periodicities in the emission of gravitational radiation and the behavior of the recoil velocity.

The remainder of this paper is organized as follows. In Sec. II we discuss our two numerical codes (LEAN and GRChombo), the computational framework, and the catalog of simulations we produced for this study. In Sec. III we present the main results of our simulations. In Sec. IV we summarize these results and point out possible directions for future work. In Appendix A we detail our tests for numerical accuracy and verify that our two codes give comparable results. Finally, in Appendix B we discuss the tagging of cells for adaptive mesh refinement used in one of our numerical codes (GRChombo). Throughout this work we use geometrical units ($G = c = 1$).

II. COMPUTATIONAL FRAMEWORK AND SET OF SIMULATIONS

A. Numerical methods

The simulations reported in this work have been performed with the GRChombo [60,61] and LEAN [62] codes. We estimate the error budget of our simulations from both codes to be up to 3.5%. Details of our convergence analyses are provided in Appendix A. Though different codes were used for each sequence of configurations, we undertook comparison tests in order to ensure consistent results, and these can also be found in Appendix A.

1. GRChombo setup

GRChombo [60] is a finite difference numerical relativity code which uses the method of lines with fourth-order Runge-Kutta time stepping. In contrast to previous studies with GRChombo, we have implemented sixth-order spatial stencils in order to improve phase accuracy [63]. The Einstein equations are solved by evolving the covariant and conformal Z4 (CCZ4) formulation [64] with the prescription described in Sec. F of Ref. [65], namely, the replacement $\kappa_1 \to \kappa_1/\alpha$, in order to stably evolve BHs and maintain spatial covariance. After this replacement and in the notation of Ref. [64], we use the constraint damping parameters $\kappa_1 = 0.1$, $\kappa_2 = 0$, and $\kappa_3 = 1$ in all simulations. However, unlike Refs. [60,64], we use the conformal factor defined by

$$\chi = \det(\gamma_{ij})^{-1/3}, \tag{1}$$

where γ_{ij} is the physical spatial metric. GRChombo is built on the Chombo [66] library for solving partial differential equations with block-structured adaptive mesh refinement (AMR) which supports nontrivial mesh hierarchies using Berger-Rigoutsos grid generation [67]. The grid comprises a hierarchy of cell-centered Cartesian meshes consisting of $L+1$ refinement levels labeled from $l = 0, \ldots, L$, each with grid spacing $h_l = h_0/2^l$. Given the AMR, the grid configuration changes dynamically during the simulation. The regridding is controlled by the tagging of cells for refinement in the Berger-Rigoutsos algorithm [67], with cells being tagged if the tagging criterion C exceeds a specified threshold value t_R. Details of the tagging criterion used in this work are provided in Appendix B. The Berger-Oliger scheme [67] is used for time stepping on the mesh hierarchy, and we take a Courant-Friedrichs-Lewy (CFL) factor of $1/4$ in all simulations. Due to the inherent symmetry of the configurations considered, we employ bitant symmetry in order to reduce the computational expense.

2. LEAN setup

The LEAN code [62] is based on the CACTUS computational toolkit [68] and uses the method of lines with fourth-order Runge-Kutta time stepping and sixth-order spatial stencils for improved phase accuracy [63]. The Einstein equations are implemented in the form of the Baumgarte-Shapiro-Shibata-Nakamura-Oohara-Kojima (BSSNOK) formulation [69–71] with the moving-puncture gauge [72,73]. The CARPET driver [74] provides AMR using the technique of "moving boxes." We use bitant symmetry to exploit the symmetry of the simulations and reduce computational expense. The computational domain comprises a hierarchy of $L+1$ refinement levels labeled from $l = 0, \ldots l_F, \ldots, L$, each with grid spacing $h_l = h_0/2^l$. Before applying the symmetry, for $l \le l_F$, each level consists of a single fixed cubic grid of half-length[1] $R_l = R_0/2^l$, and for $l_F < l \le L$ each level consists of two cubic components of half-length $R_l = 2^{L-l}R_L$ centered around each BH. We adopt this notation for consistency with that used to describe GRChombo. This translates into the more conventional LEAN grid setup notation (cf. Ref. [62]) as

$$\{(R_0, \ldots, 2^{-l_F}R_0) \times (2^{L-l_F-1}R_L, \ldots, R_L), h_L\}. \tag{2}$$

A CFL factor of $1/2$ is used in all simulations, and apparent horizons are computed with AHFinderDirect [75,76].

3. Initial data

For both codes, we use puncture data [77] of Bowen-York [78] type provided by the spectral solver of Ref. [79] in the form of the CACTUS thorn TwoPunctures for LEAN, and a standalone version integrated into GRChombo. In the latter case, we take advantage of the improvements made in Ref. [80] to use spectral interpolation.

B. Black-hole binary configurations

We follow the construction of sequences of BH binary configurations and the notation of Ref. [81]. In particular, we denote by M_1 and M_2 the initial BH masses. Without loss of generality, since we are only considering unequal masses ($M_1 \neq M_2$), we take $M_2 > M_1$ and denote their sum by $M = M_1 + M_2$. The reduced mass is $\mu = M_1 M_2/M$, and to quantify the mass ratio we use either

$$q = \frac{M_1}{M_2} \tag{3}$$

or the symmetric mass ratio $\eta = \mu/M$. Finally, the total Arnowitt-Deser-Misner (ADM) mass [82] is denoted by $M_{\rm ADM}$.

In order to construct a sequence for a fixed mass ratio, we first determine an initial quasicircular configuration. We specify the initial coordinate separation D/M along the x axis, and the scale in the codes is fixed by choosing $M_1 = 0.5$. Next, Eq. (65) in Ref. [83] is used to calculate the initial tangential momentum of each BH, $\mathbf{p} = (0, \pm p, 0)$ (as shown in Fig. 1). We use a Newton-Raphson method to iteratively solve for the Bowen-York bare mass parameters that give the desired BH masses. The binding energy of this quasicircular configuration is then computed using

$$E_{\rm b} = M_{\rm ADM} - M. \tag{4}$$

The rest of the sequence with increasing orbital eccentricity is constructed by fixing the binding energy and gradually

[1] In one departure from this rule, we enhance R_2 by a factor of $4/3$ for the simulations of sequence `lq1:2` of Table I.

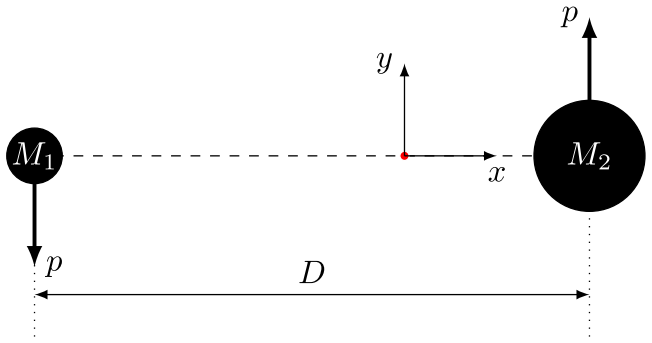

FIG. 1. Schematic diagram of the initial BH binary setup for an arbitrary configuration in one of the sequences.

reducing the initial linear momentum parameter p. We decide to reduce the linear momentum rather than, for example, altering its direction, so that the x axis is fixed as the initial apoapsis for all configurations. For a given configuration with fixed p, we iteratively solve for the separation D and bare masses that give the required binding energy and BH masses. The choice to keep the binding energy constant as the momentum parameter (and thus the initial kinetic energy) is reduced means that the initial separation increases along the sequence. This ensures an inspiral phase of comparable duration as the eccentricity increases. The initial orbital angular momentum of the system is given by $L = Dp$ [84]. Even though D increases as p decreases, the initial angular momentum of the system monotonically decreases as p decreases for all but the least one or two eccentric configurations in a sequence.

We have parametrized the configurations within a sequence by their initial tangential momentum p, but we would like to measure the eccentricity of these configurations. Unfortunately, there is no gauge-invariant measure of eccentricity [85] and the ambiguity in any definition is particularly pronounced in the late stages of inspiral from which our simulations start. Following Ref. [81], we use the formalism in Ref. [86] to obtain a PN estimate for the eccentricity. Note that this formalism has three eccentricity parameters—e_t, e_r, and e_ϕ—and employs two different types of coordinates: ADM-like and harmonic. The choice of which parameter and coordinate type to use is somewhat arbitrary. We mostly focus on the eccentricity parameter e_t in harmonic coordinates,[2] as in Ref. [42]. This estimate should be taken with a pinch of salt due to the relatively small initial binary separations D in our simulations. Furthermore, e_t has an infinite gradient as a function of the initial orbital angular momentum in the quasicircular limit (see Fig. 1 in Ref. [81]), such that values of $e_t \lesssim 0.1$ are difficult to realize in practice, unless the BHs start from a large initial distance. In the head-on limit e_t diverges, and a Keplerian/Newtonian interpretation ceases to be valid. Despite these shortcomings, this estimate provides us with a helpful approximation of the eccentricity and a criterion to quantify deviations away from quasicircularity.

[2]The ADM-like estimate of Ref. [86] differs by only a few percent for $e_t \lesssim 0.8$, and would not significantly alter our results.

TABLE I. Sequences of binary BH configurations studied in this work with their mass ratio, binding energy E_b/M, and the GW extraction radius r_{ex}. For reference, we also list for each sequence the kick velocities v_c in the quasicircular limit. These values agree, within the numerical uncertainties, with the results of Ref. [21].

Sequence	Code	q	E_b/M	r_{ex}/M	v_c (km/s)
`sq2:3`	GRChombo	2/3	−0.0113386	88	102
`sq1:2`	LEAN	1/2	−0.0106964	80	149
`lq1:2`	LEAN	1/2	−0.0090858	80	150
`sq1:3`	GRChombo	1/3	−0.0093684	65	178

TABLE I. Sequences of binary BH configurations studied in this work with their mass ratio, binding energy E_b/M, and the GW extraction radius r_{ex}. For reference, we also list for each sequence the kick velocities v_c in the quasicircular limit. These values agree, within the numerical uncertainties, with the results of Ref. [21].

The sequences considered in this work are given in Table I. Note that there are two sequences corresponding to the mass ratio $q = 1/2$. The sequence `lq1:2` has a longer inspiral phase compared to the other sequences. For the nearly quasicircular configurations, the binary completes about six orbits before merger in the `lq1:2` sequence, and about three orbits in all other sequences. The longer sequence of simulations was conducted in order to identify any possible artifacts in the shorter sequences due to the exclusion of the earlier inspiral phase. In addition to the labeling of sequences in Table I, we refer to individual simulations within a sequence by appending "`-p`" to the sequence label, followed by a four digit integer which is given by $10^3 p/M$ truncated appropriately; for example, `sq1:2-p0100` denotes the simulation in sequence `sq1:2` with initial tangential momentum $p = 0.1M$.

C. Diagnostics

For all simulations, we have extracted values of the Weyl scalar Ψ_4 on spheres of finite coordinate radius given in Table I for each sequence. We also computed the dominant terms in the multipolar decomposition,

$$\Psi_4(t, r, \theta, \phi) = \sum_{\ell=2}^{\infty} \sum_{m=-\ell}^{\ell} \psi_{\ell,m}(t, r)[{}_{-2}Y^{\ell,m}(\theta, \phi)], \quad (5)$$

where ${}_{-2}Y^{\ell,m}$ are the usual spin-weight -2 spherical harmonics.

Our main diagnostics are the energy, linear momentum, and angular momentum radiated in GWs, which are computed directly from the extracted Ψ_4 values on the spheres using standard methods. For completeness, we reproduce the formulas here.

The radiated energy E^{rad} is given by [87,88]

$$E^{rad}(t) = \lim_{r\to\infty} \frac{r^2}{16\pi} \int_{t_0}^{t} dt' \oint_{S_r^2} d\Omega \left| \int_{-\infty}^{t'} dt'' \Psi_4 \right|^2. \quad (6)$$

The radiated linear momentum $\mathbf{P}^{\rm rad}$ is given by

$$\mathbf{P}^{\rm rad}(t) = \lim_{r\to\infty} \frac{r^2}{16\pi} \int_{t_0}^{t} dt' \oint_{S_r^2} d\Omega \hat{\mathbf{e}}_r \left| \int_{-\infty}^{t'} dt'' \Psi_4 \right|^2, \quad (7)$$

where $\hat{\mathbf{e}}_r$ is the flat-space unit radial vector

$$\hat{\mathbf{e}}_r = (\sin\theta\cos\phi, \sin\theta\sin\phi, \cos\theta). \quad (8)$$

Finally, the radiated angular momentum $\mathbf{J}^{\rm rad}$ is given by

$$\mathbf{J}^{\rm rad}(t) = -\lim_{r\to\infty} \frac{r^2}{16\pi} \mathrm{Re} \int_{t_0}^{t} dt' \left\{ \oint_{S_r^2} \left(\int_{-\infty}^{t'} dt'' \bar{\Psi}_4 \right) \times \hat{\mathbf{J}} \left(\int_{-\infty}^{t'} dt'' \int_{-\infty}^{t''} dt''' \Psi_4 \right) d\Omega \right\}, \quad (9)$$

where the angular momentum operator $\hat{\mathbf{J}}$ for spin weight $s = -2$ is given by

$$\hat{\mathbf{J}} = \left(\mathrm{Re}\hat{\mathbf{J}}_+, \mathrm{Im}\hat{\mathbf{J}}_+, \frac{\partial}{\partial\phi} \right), \quad (10)$$

and

$$\hat{\mathbf{J}}_+ = e^{i\phi} \left(i\frac{\partial}{\partial\theta} - \cot\theta \frac{\partial}{\partial\phi} + 2i\csc\theta \right). \quad (11)$$

Additionally, we compute the radiated linear momentum from the multipolar amplitudes $\psi_{\ell,m}$ in Eq. (5) using the formulas of Ref. [89]. From the symmetry of our configurations, the z component vanishes identically: $P_z^{\rm rad} = 0$. For the components in the orbital plane, we write $P_+^{\rm rad} = P_x^{\rm rad} + iP_y^{\rm rad}$. Then,

$$P_+^{\rm rad}(t) = \sum_{\tilde{\ell}=2}^{\infty} \sum_{\tilde{m}=-\tilde{\ell}}^{\tilde{\ell}} P_+^{\tilde{\ell},\tilde{m}}, \quad (12)$$

where

$$P_+^{\tilde{\ell},\tilde{m}}(t) = \lim_{r\to\infty} \frac{r^2}{8\pi} \int_{t_0}^{t} dt' \left\{ \left(\int_{-\infty}^{t'} dt'' \psi_{\tilde{\ell},\tilde{m}} \right) \times \left(\int_{-\infty}^{t'} [a_{\tilde{\ell},\tilde{m}} \bar{\psi}_{\tilde{\ell},\tilde{m}+1} + b_{\tilde{\ell},-\tilde{m}} \bar{\psi}_{\tilde{\ell}-1,\tilde{m}+1} - b_{\tilde{\ell}+1,\tilde{m}+1} \bar{\psi}_{\tilde{\ell}+1,\tilde{m}+1}] dt'' \right) \right\}, \quad (13)$$

and the coefficients $a_{\ell,m}$ and $b_{\ell,m}$ are given by

$$a_{\ell,m} = \frac{\sqrt{(\ell-m)(\ell+m+1)}}{\ell(\ell+1)}, \quad (14)$$

$$b_{\ell,m} = \frac{1}{2\ell} \sqrt{\frac{(\ell-2)(\ell+2)(\ell+m)(\ell+m-1)}{(2\ell-1)(\ell+1)}}. \quad (15)$$

We will find it helpful to define the partial sums,

$$P_+^{\tilde{\ell}} = \sum_{\tilde{m}=-\tilde{\ell}}^{\tilde{\ell}} P_+^{\tilde{\ell},\tilde{m}}, \quad (16)$$

$$P_+^{\leq\tilde{\ell}} = \sum_{\tilde{\ell}'=2}^{\tilde{\ell}} P_+^{\tilde{\ell}'}. \quad (17)$$

In practice, we do not evaluate the limit in Eqs. (6), (7), (9), and (13), but rather just evaluate them at the finite extraction radius $r = r_{\rm ex}$, as given in Table I. A discussion of the error this introduces is given in Appendix A.

In order to exclude the spurious radiation inherent in Bowen-York initial data, we start the integration in Eqs. (6), (7), (9), and (13) at $t_0 = 50M + r_{\rm ex}$. The recoil velocity is computed from the radiated momentum according to

$$\mathbf{v} = -\frac{\mathbf{P}^{\rm rad}}{M_{\rm fin}}, \quad (18)$$

where $M_{\rm fin}$ is the mass of the BH merger remnant. The quantity $M_{\rm fin}$ can be computed using energy balance:

$$M_{\rm fin} = M_{\rm ADM} - \tilde{E}^{\rm rad}, \quad (19)$$

where $\tilde{E}^{\rm rad}$ denotes the radiated energy *including* the spurious radiation. We similarly compute the spin of the final BH $\chi_{\rm fin}$ (which, by symmetry, must be in the z direction) using the radiated angular momentum:

$$\chi_{\rm fin} = \frac{L - J_z^{\rm rad}}{M_{\rm fin}^2}, \quad (20)$$

where the initial angular momentum is $L = pD$. For LEAN simulations, we have compared $M_{\rm fin}$ and $\chi_{\rm fin}$ with the corresponding values derived from the apparent horizon properties, and find agreement to within $\leq 0.1\%$.

III. RESULTS

Using the framework summarized in the previous section, we have simulated four sequences of nonspinning BH binaries, characterized by their mass ratio (3) and binding energy (4). The parameters of these sequences are listed in Table I. We have selected our mass ratios such that they cover the regime of maximum recoil, realized for $\eta = 0.195$ or $q = 1/2.77$ (cf. Fig. 3). Recall that sequences `sq2:3`, `sq1:2`, and `sq1:3` complete about three orbits and sequence `lq1:2` completes about six orbits, respectively, in the quasicircular limit.

Our main results are displayed in Fig. 2, where we plot for all sequences the total recoil speed $v_{\rm tot}$, various truncations of the multipolar contributions to the total

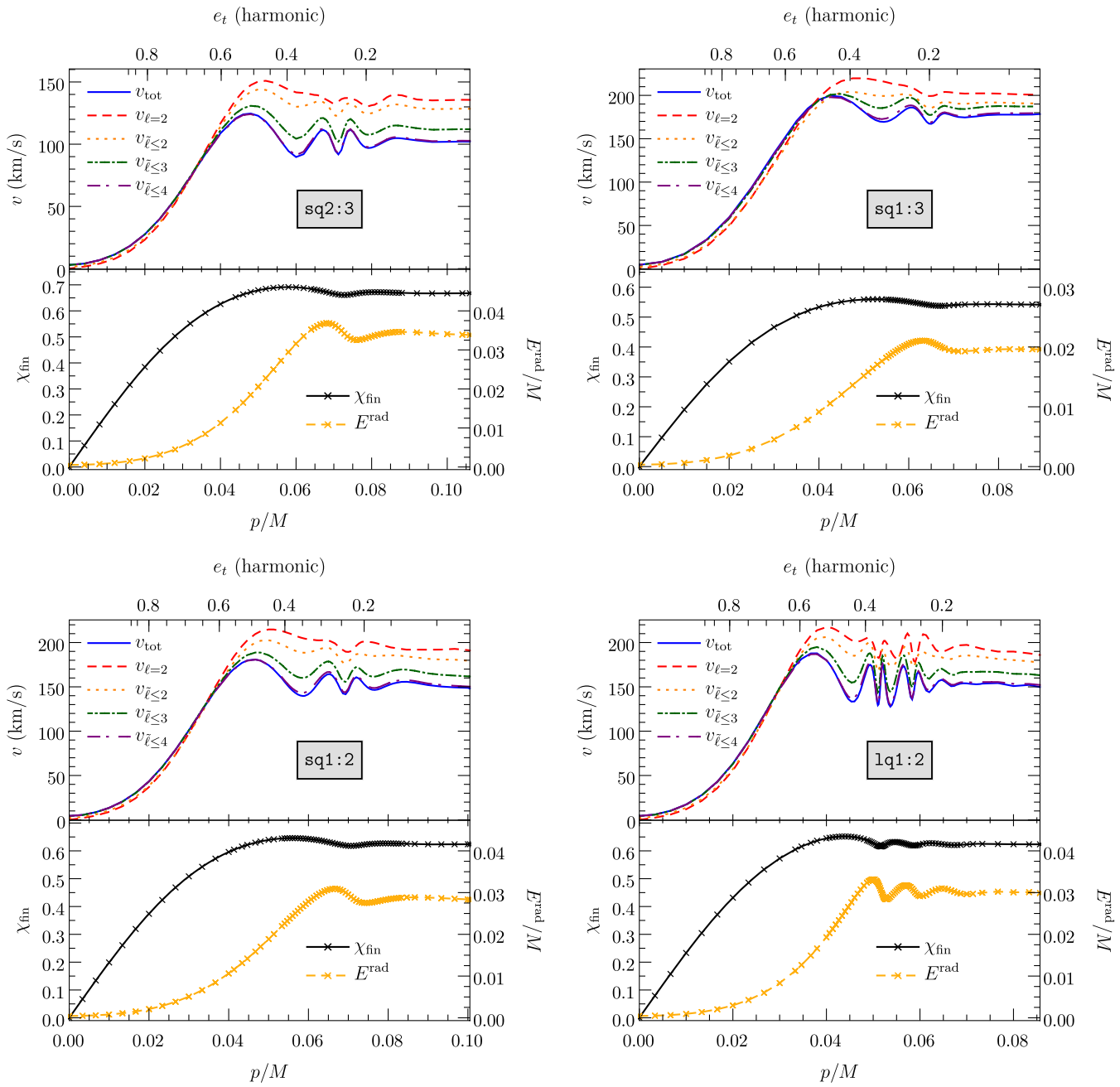

FIG. 2. For each sequence of simulations in Table I: Top panel: the recoil velocity v is plotted as a function of the initial tangential momentum p/M. The individual curves represent the total kick $v_{\rm tot}$ (blue, solid), the contribution to the kick from $\ell = 2$ modes of Ψ_4, ψ_{2m}, only in Eqs. (12)–(13) $v_{\ell=2}$ (red, dashed), and the contributions to the kick from $P_+^{\leq\tilde{\ell}'}$ defined in Eq. (17) $v_{\tilde{\ell}\leq\tilde{\ell}'}$ for $\tilde{\ell}' = 2$ (orange, dotted), $\tilde{\ell}' = 3$ (green, dot-dashed), and $\tilde{\ell}' = 4$ (purple, long dot-dashed). Our estimate of the eccentricity (see Sec. II B) is provided on the upper horizontal axis. Bottom panel: the final BH spin $\chi_{\rm fin}$ (black, solid) and the energy radiated in GWs $E^{\rm rad}$ (gold, dashed) are also plotted as functions of p/M. For both curves, the individual simulations performed for this analysis are shown by $\times$ symbols.

recoil according to Eqs. (12)–(17), the total radiated GW energy $E^{\rm rad}$, and the dimensionless spin $\chi_{\rm fin}$ of the BH resulting from the merger.

Let us first focus on the total recoil $v_{\rm tot}$, displayed in each of the figure's top panels as the blue solid line. For each mass ratio, the global maximum of the kick velocity is realized for moderate eccentricities $e_t \approx 0.5$. We also illustrate this kick variation in Fig. 3, where the solid blue curve shows the quasicircular kick as a function of the symmetric mass ratio η according to Fit 3 in Table V of Ref. [90]. The velocity ranges obtained for our eccentric binaries are overlayed as the vertical bars for each of our

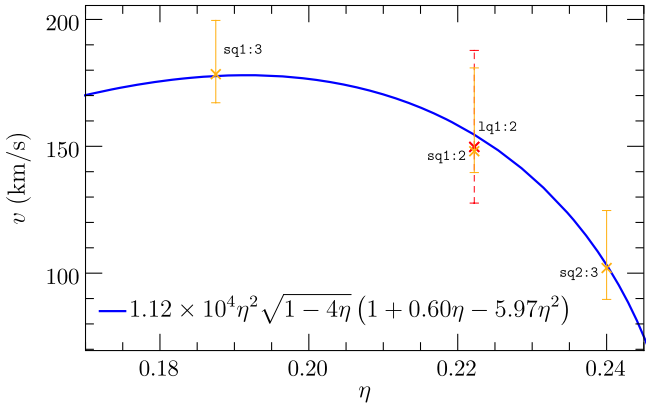

FIG. 3. The range of recoil velocities obtained for each sequence is plotted against the symmetric mass ratio η. Note that for each sequence we exclude the configurations with $p < p_{\rm max}$ (i.e., the head-on limit), where $p = p_{\rm max}$ is the tangential momentum that maximizes the kick. The three short sequences are marked in gold and the long sequence is marked in red (dashed). A fitted formula for the quasicircular kick as a function of η from Ref. [90] is also shown in blue for comparison.

sequences. The bar for each constant-η sequence is obtained by starting at the quasicircular limit on the right of each panel in Fig. 2 and identifying the minimum and maximum of $v(p)$, excluding the plunge regime to the left of the global maximum.

For our sequences `sq2:3`, `sq1:2`, and `lq1:2`, the magnification of the kick through moderate values of the orbital eccentricity is similar to the enhancement by up to 25% reported in Ref. [42] for the so-called superkick configurations [23,24]. For `sq1:3` the effect is milder, with a ∼12% amplification, but still well above the uncertainty estimates of our simulations. On the other hand, as evidenced by the oscillatory pattern of the function $v(p)$ in Fig. 2, appropriate nonzero values of the eccentricity can also lead to a *reduction* of the maximum kick at a given mass ratio by ∼10%. This overall modification of the gravitational recoil in the merger of eccentric, nonspinning BH binaries is the first main result of our study.

Besides the global maximum, we also note a number of local minima and maxima in the kick velocity as we vary the eccentricity in Fig. 2. For all mass ratios ($q = 2/3, 1/2, 1/3$) we see about five local extrema in $v(p)$ in our three short sequences, corresponding to the two upper panels and the bottom-left panel. We notice a similar, albeit less pronounced oscillatory pattern in the functions $E_{\rm rad}(p)$ and $\chi_{\rm fin}(p)$ for the radiated energy and final spin in the lower subpanels in Fig. 2. Our results display no systematic correlation, however, between the extrema of the respective quantities; neither global nor local extrema in v, $E_{\rm rad}$, or $\chi_{\rm fin}$ coincide in magnitude or their eccentricity values. We believe this diversity is due to the qualitatively different dependence of the radiated quantities on the GW multipoles: overlaps of *different* multipoles for the kick, a sum of terms $\propto \psi_{lm}^2$ for the energy, and the interaction of first and second time integrals for the angular momentum in Eq. (9).

We added to our study the $q = 1/2$ sequence of longer BH binary inspirals to investigate whether these anomalies in $v = v(p)$ might merely result from ignoring in our simulations the earlier inspiral phase. The remarkable outcome of this test, however, is that the oscillatory behavior in the kick as a function of eccentricity is *more* pronounced in the long sequence. The solid blue curve in the bottom-right panel of Fig. 2 displays significantly more rapid oscillations in the eccentricity regime $0.2 \lesssim e_t \lesssim 0.4$ as compared to the shorter inspiral sequences. This oscillatory behavior, and the apparent increase in the number of oscillations as we increase the initial separation of the BHs, is the second of our results.

We next attempt to gain insight into the origin of this behavior. For this purpose, we have computed the multipolar contributions to the total kick according to Eqs. (13)–(17). The resulting velocities are displayed in Fig. 2 by the additional dashed, dotted, and dash-dotted curves. Here, the curves labeled $v_{\ell=2}$ have been computed from the $\ell = 2$ modes of Ψ_4 ($\psi_{2,m}$ only) in Eqs. (12)–(13). We computed this additional contribution (red dashed curves in the figure) to determine whether the oscillatory behavior is also present in the pure quadrupole signal. The answer is yes: the oscillations are clearly perceptible in $v_{\ell=2}$, even though they are a bit milder than in the total kick $v_{\rm tot}$. Considering all (cumulative) multipolar contributions shown in Fig. 2, we notice the following behavior:

(1) The oscillatory dependence of the kick on eccentricity is present at any level of truncating the multipolar contributions in the cumulative sum (17).
(2) The partial sum of the kick up to $\tilde{\ell} = 4$ barely differs from the total kick, indicating that higher-order overlap terms do not significantly contribute to the kick.
(3) The higher-order contributions $\tilde{\ell} > 2$ to the cumulative kick (17) systematically decrease the kick, counteracting the pure quadrupole contribution $v_{\ell=2}$.

In short, we have not identified any specific multipoles dominating the variation in the kick function $v = v_{\rm tot}(p)$.

In our search for an explanation, we turn next to the infall direction of the BH binary just before merger. A well-known feature of the superkicks generated in the inspiral of BHs with opposite spins $\boldsymbol{S}_1 = -\boldsymbol{S}_2$ pointing in the orbital plane is the sinusoidal variation with the initial azimuthal angle of the spin vectors; cf. Fig. 4 in Ref. [91]. The initial orientation of the spins can, alternatively, be interpreted as a measure for the angle between the in-plane spin components and the BH binary's infall direction at merger [92]. The superkick is therefore commonly determined by simulating otherwise identical BH binary configurations for different values of this angle and fitting the resulting

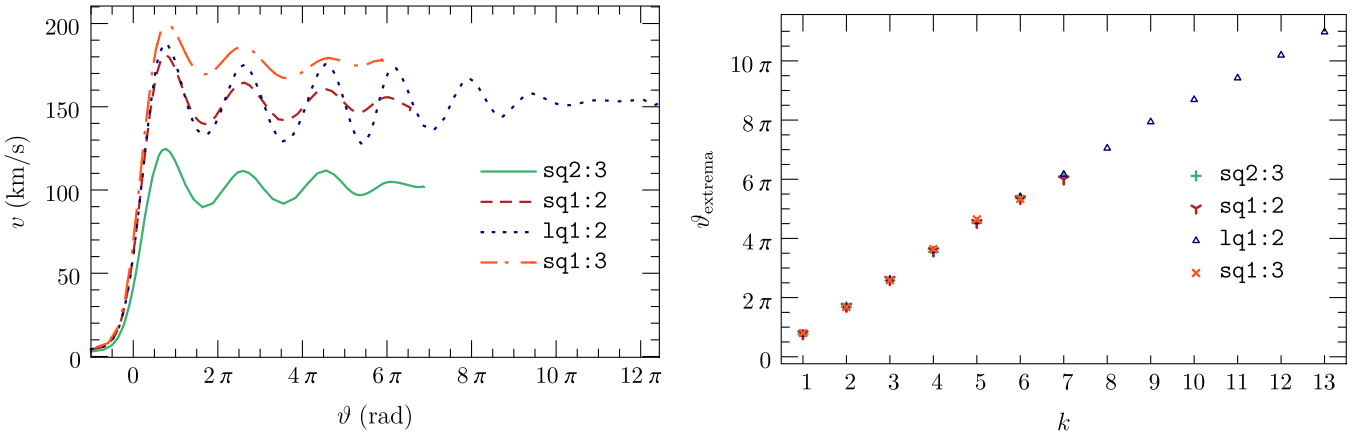

FIG. 4. Plots involving the angle of the kick ϑ for all sequences. In the left panel we plot the BH recoil velocity v against ϑ. In the right panel we plot the location of the local extrema $\vartheta_{\text{extrema}}$ of the left panel against the index of the extrema k counting rightwards from the global maximum on the left.

data with a cosine function; see, e.g., Sec. III A in Ref. [42]. For the eccentric, nonspinning BH binaries considered in this work, it is the initial apsis (either a periapsis or an apoapsis) that defines a reference direction. Unfortunately, neither the apsis nor a "binary infall direction" are rigorously defined quantities in the strong-field regime of general relativity, and we consider instead the orientation of the final kick relative to the x axis, defined by

$$\tilde{\vartheta} = \arg(v_x + \mathrm{i}v_y). \tag{21}$$

For convenience, we define

$$\vartheta = \tilde{\vartheta} + 2n\pi, \tag{22}$$

where $n \geq 0$ is chosen minimally for each configuration in order to obtain ϑ as a monotonic function of the initial tangential momentum p for each sequence. We will interchangeably refer to ϑ and $\tilde{\vartheta}$ as the angle of the kick. Since all of our simulations start with the BHs located on the x axis with purely tangential initial momentum $\mathbf{p} = (0, \pm p, 0)$ (Fig. 1), the x direction can be regarded as the initial direction of the apoapsis. If we furthermore interpret the gravitational recoil to be predominantly generated by the excess beaming of the GWs in the direction of the smaller and faster BH (see Fig. 3 in Ref. [93]) during the short merger phase, the kick direction can serve as an approximate measure for the infall direction of the binary.

We can test this prediction by computing the kick magnitude as a function of the angle ϑ; if correct, we would expect a periodic variation with a period close to 2π. We do not expect an exact 2π periodicity because the relevant periapsis (or apoapsis) direction should be the last one before merger, and will shift away from the x axis during the inspiral due to apsidal precession—the BH analog of Mercury's perihelion precession around the Sun. More specifically, we would expect deviations from a 2π periodicity to be more pronounced for longer inspirals, i.e., lower eccentricity and/or larger initial separations, but only mildly dependent on the mass ratio q. Quite remarkably, all of these features are borne out by the functions $v = v(\vartheta)$ displayed for our four sequences in the left panel of Fig. 4 and the location of the extrema in this plot shown in the right panel of Fig. 4. For all sequences we observe the same approximate 2π periodicity, with deviations from this value increasing at larger ϑ, i.e., for longer inspirals. Note also that $\vartheta = -\pi$ in the head-on limit, as expected for our initial configurations, that start with the heavier BH located on the positive x axis.

While short of a rigorous proof, this result provides considerable evidence in favor of interpreting the oscillatory dependence of the kick on the eccentricity as a consequence of the corresponding variation in the infall direction as measured relative to the last apoapsis (or periapsis) of the eccentric binary. This interpretation also explains why the longer sequence `lq1:2` exhibits more oscillations than the shorter sequences `sq1:3`, `sq1:2`, and `sq2:3`. Let us consider for this purpose two binary configurations that only differ by a tiny amount of eccentricity δe. The longer the inspiral phase, the more time these two binaries have to build up a considerable phase difference and, hence, a different kick and merger GW signal. Note the potentially dramatic consequences of this behavior for the GW emission from eccentric binaries over astrophysical time scales. For long astrophysical inspirals retaining some eccentricity near merger, the kick and GW merger signal should exhibit critical dependence on the eccentricity. In terms of our Fig. 2, the function $v = v(e_t)$ would display a huge number of oscillations rather than the handful observed in our case, and the resulting curve would look like a "band" rather than a single line. Within the band, a very small change δe_t in eccentricity can produce a finite change in the kick and merger waveform.

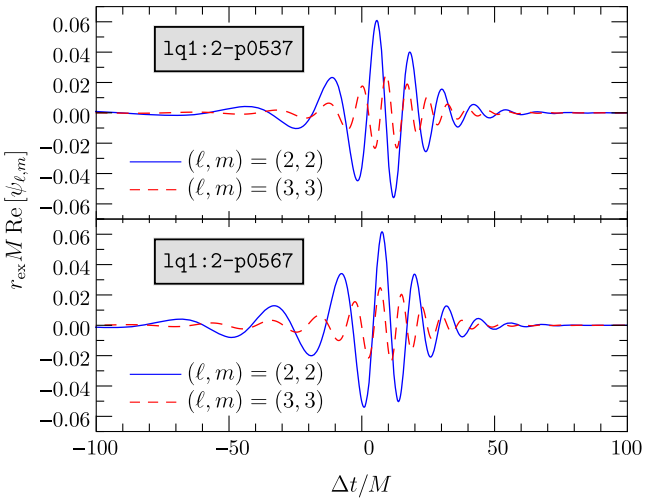

FIG. 5. The real parts of the $(\ell, m) = (2, 2)$ and (3,3) modes of Ψ_4 are shown as functions of time for the two binaries of sequence `lq1:2` with $p/M = 0.537$ and $p/M = 0.567$, resulting in kick velocities of $v = 128$ and 173 km/s, respectively.

As indicated by our analysis of the multipolar contributions to the total recoil, the variations in the GW signal are of a complex nature. We defer a more comprehensive analysis of the GW pattern to future work, but merely illustrate with an example the type of variations that are encountered. For this purpose, we show in Fig. 5 the $(\ell, m) = (2, 2)$ and (3,3) multipoles of the GW signal around merger for the configurations `lq1:2-p0537` and `lq1:2-p0567`, corresponding to a local minimum and maximum in the kick, respectively; cf. the bottom-right panel of Fig. 2. In Fig. 5, the time has been shifted such that $\Delta t = 0$ corresponds to the first occurrence of a common apparent horizon. The main difference perceptible in the figure is the relative phase shift of the (3,3) mode relative to the dominant quadrupole (2,2). For the case $p = 0.567M$ with maximal kick, the global peaks of both multipoles are aligned, whereas for $p = 0.537M$ with minimal kick, the global peak of the (2,2) mode coincides with a minimum in $(\ell, m) = (3, 3)$. We have made similar observations for other pairs of modes such as (2,2) and (2,1), and find these pairs to dominate the oscillatory variation in the multipolar series expansion (17).

IV. CONCLUSIONS

In this paper we have studied the gravitational recoil and GW emission of sequences of nonspinning BH binaries with mass ratios $q = 2/3$, $1/2$, and $1/3$, and eccentricity varying from the quasicircular to the head-on limit. For this purpose we have evolved 274 configurations with the GRChombo and LEAN codes. Both codes yield convergent results for the recoil with a total error budget of 3–4% and exhibit excellent agreement, well within this uncertainty estimate, for a verification configuration simulated with both codes. In order to estimate the impact of variations in the overall length of the inspirals, we have evolved two sequences for the case $q = 1/2$ which complete about three and six orbits, respectively, in the quasicircular limit.

The findings of our study are summarized as follows.

(i) For all sequences, the total recoil reaches a global maximum for moderate eccentricities $e \sim 0.5$. As in the case of the enhancement of superkicks studied in Ref. [42], the maximum kick is enhanced by up to about 25% relative to the value obtained for quasicircular configurations.

(ii) Besides this global maximum, we observe an oscillatory dependence of the kick v as a function of eccentricity, with several local minima and maxima in the function $v = v(e)$. Appropriate nonzero values of the eccentricity can lead to a *reduction* of the kick by ~10% relative to the quasicircular value instead of an increase. By splitting the kick into separate multipolar contributions, we notice that this oscillatory dependence is already present, albeit in a slightly weaker form, when we consider only quadrupole terms in the series expansion (12). Further contributions involving $\ell \geq 2$ multipoles tend to decrease the overall kick and mildly enhance the oscillatory variation; see Fig. 2.

(iii) We interpret this oscillatory variation in the kick as a consequence of changes in the angle between the infall direction at merger and the apoapsis (or periapsis) direction. In the absence of rigorous definitions for either of these directions, we approximate this angular variation by considering the direction of the final kick and the x axis, assuming that the former is related via relativistic GW beaming to the infall direction and by taking into account that our BHs start on the x axis with zero radial momentum. Displayed as a function of this angle, the kick displays the expected periodic behavior with a period close to but mildly deviating from 2π, presumably due to periapsis precession.

(iv) We have explored the dependence of this oscillatory behavior of the recoil by simulating an additional sequence of eccentric binaries with mass ratio $q = 1/2$, but less negative binding energy, corresponding to about six orbits in the quasicircular limit. We find the oscillations in $v = v(e)$ to be more pronounced and numerous than in the shorter sequence. We attribute this feature to the longer available time window during which otherwise identical binaries with tiny differences in the initial eccentricity build up a phase difference prior to merger. This observation raises the intriguing possibility that the total recoil depends highly sensitively on the initial eccentricity.

(v) The variations in the kick velocity are accompanied by relative time shifts in the peak amplitudes of

subdominant multipoles relative to the peaks of the (2,2) mode; cf. Fig. 5. For configurations with a large (small) kick, the peak amplitude of subdominant multipoles tends to be aligned (misaligned) with the quadrupole peak.

Our findings point to a variety of future investigations. While our simulations indicate an increased sensitivity of the GW merger signal to the initial eccentricity for larger initial separations (i.e., longer inspirals), it is not clear how this will be affected by the circularizing nature of GW emission. In this context, it will also be important to analyze in more quantitative terms the differences in the GW signals and possible implications for parameter inference in GW observations. A thorough investigation of long eccentric inspirals on astrophysical time scales will likely require PN methods and may benefit greatly from a multi-time-scale analysis in phase space, as applied to spin-precessing BH binaries in Refs. [94,95] or to the dynamics of binary systems in external gravitational background potentials in Refs. [96,97]. If there is a single conclusion to draw from the results of this work, it is the surprisingly rich phenomenology of the GW signals of eccentric compact binaries—even in the absence of spins—which merits as much as it requires further investigation.

ACKNOWLEDGMENTS

We thank Michalis Agathos, Vishal Baibhav, Vitor Cardoso, Thomas Helfer, and Nicholas Speeney for useful discussions. We also thank Chris Moore, Carlos Lousto, and Juan Calderón Bustillo for helpful comments on this manuscript. M. R. thanks the GRChombo collaboration [61] for their code development, and particularly Katy Clough and Tiago França. M. R. is supported by a Science and Technology Facilities Council (STFC) studentship. U.S. is supported by the European Union's H2020 ERC Consolidator Grant "Matter and strong-field gravity: new frontiers in Einstein's theory" Grant No. MaGRaTh–646597, and the STFC Consolidator Grant No. ST/P000673/1. E. B. is supported by NSF Grant No. PHY-1912550, NSF Grant No. AST-2006538, NASA ATP Grant No. 17-ATP17-0225, and NASA ATP Grant No. 19-ATP19-0051. This work has received funding from the European Union's Horizon 2020 research and innovation programme under the Marie Skłodowska-Curie Grant No. 690904. This work was supported by the GWverse COST Action CA16104, "Black holes, gravitational waves and fundamental physics." Computational work was performed on the San Diego Supercomputer Center Comet and Texas Advanced Computing Center (TACC) Stampede2 clusters at the University of California San Diego and the University of Texas at Austin (UT Austin), respectively, through NSF-XSEDE Grant No. PHY-090003; the Cambridge Service for Data Driven Discovery (CSD3) system at the University of Cambridge through STFC capital Grants No. ST/P002307/1 and No. ST/R002452/1, and STFC operations Grant No. ST/R00689X/1; the TACC Frontera cluster at UT Austin; and the JUWELS cluster at GCS@FZJ, Germany through PRACE Grant No. 2020225359.

APPENDIX A: NUMERICAL ACCURACY

As in Ref. [42], the uncertainty in our numerical results for the recoil velocities has two predominant contributions: the discretization error and the finite extraction radii for the Weyl scalar Ψ_4.

To estimate the uncertainty arising from the latter, we have selected a representative sample of the simulations from each sequence and extrapolated the cumulative radiated momentum to infinity from about six extraction radii in the range $r_{\rm ex}/2 \leq r_{\rm ex}$ using a Taylor series in $1/r$ as in Ref. [98]. We report the results from the finite extraction radii given in Table I and estimate the error by comparing with the linear-order extrapolation. For both codes, we estimate that the contribution from this error is about 2% for all sequences.

In order to estimate the error contribution from finite differencing and verify that our codes give consistent results, we have performed simulations of `sq1:2-p0100` (the binary in sequence `sq1:2` with $p/M = 0.1$) with both codes. We discuss the analyses of the convergence of each code separately before comparing.

1. GRChombo convergence

For GRChombo, we have performed the simulations of `sq1:2-p0100` with resolutions $h_L = 3M_1/80$, $3M_1/92$, and $3M_1/104$, and we refer to the configurations corresponding to these resolutions as R1, R2, and R3, respectively. The full grid configurations are given in Table II and the results of this analysis are shown in the left panel of Fig. 6. Around merger, at $(t - r_{\rm ex})/M \sim 420$, our results exhibit mild overconvergence in the top-left panel of Fig. 6. The important results for our analysis in Fig. 2, however, are the final kick values after the merged BH has settled down. As can be seen from the inset, the convergence here is close to fifth order. From our convergence analysis, the difference between the result obtained from the R1

TABLE II. Grid configurations used for GRChombo simulations. As explained in Sec. II A 1 and Appendix B, the total number of refinement levels is $L + 1$, the number of cells along each dimension on the coarsest level is N, t_R is the regridding threshold value, b is the BH tagging buffer parameter that we set proportional to the mass M_i ($i = 1, 2$) of the nearest BH for all configurations except R4, and h_L denotes the grid spacing.

Label	L	N	t_R	b	h_L/M_1	Tagging
R1	7	320	0.012	$0.5M_i$	3/80	Spherical
R2	7	368	0.01043	$0.5M_i$	3/92	Spherical
R3	7	416	0.00923	$0.5M_i$	3/104	Spherical
R4	7	352	0.01091	0.7	3/88	Box

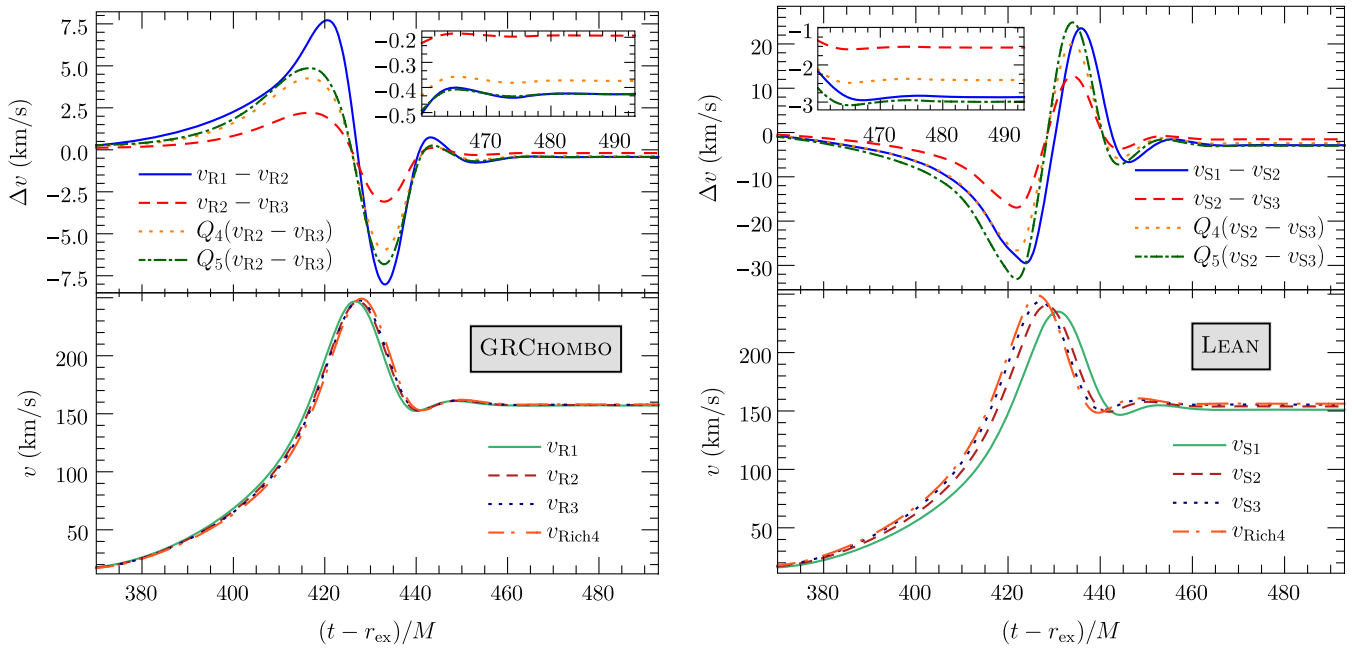

FIG. 6. For each code, we show convergence plots for the accumulated linear momentum radiated from `sq1:2-p0100` by plotting the BH recoil velocity in the bottom panels. The Richardson extrapolated curve, v_{Rich4}, assuming fourth-order convergence, is also shown in the bottom panel. The grid configurations are given in Table II for GRChombo and in Table III for LEAN. The top panel shows the difference between the configurations along with rescalings corresponding to fourth- and fifth-order convergence. The inset shows a magnification of the right side of the plot; the final value of the recoil velocity is what we show in Fig. 2.

simulation and the more conservative fourth-order Richardson-extrapolated result leads to an estimate of the discretization error of about 1%. A similar error estimate is also obtained for the radiated energy, E^{rad}. From experience, we have found smaller values for the mass ratio $q < 1$ more challenging to accurately simulate than larger values, and we therefore feel justified in using this error estimate (for a $q = 1/2$ configuration) as a conservative estimate for the error in the `sq2:3` sequence simulations ($q = 2/3$). We therefore used the R1 grid configuration for this sequence with $l_1^{\mathrm{max}} = l_2^{\mathrm{max}} = L = 7$ (both BHs are covered by the finest level; see Appendix B for details).

For the `sq1:3` simulations, we used the R4 grid configuration (see Table II) with $l_1^{\mathrm{max}} = L = 7$ and $l_2^{\mathrm{max}} = L - 1 = 6$ (the larger BH is not covered by the finest level; see Appendix B for details). This corresponds to a resolution of $h_L = 3M_1/88$. We performed a separate convergence analysis of `sq1:3-p0089`, which led to an estimated 1% discretization error.

Combining both the finite extraction radius and discretization errors, our estimate for the total error budget of the GRChombo simulations is about 3%.

2. LEAN convergence

With LEAN, we have simulated `sq1:2-p0100` with resolutions $h_L = M_1/20$, $M_1/24$, and $M_1/32$. We refer to these grid configurations as S1, S2, and S3, respectively (cf. Table III). The right panel of Fig. 6 shows convergence between fourth and fifth order. For simulations in `sq1:2`, we used the S2 grid configuration. From the convergence analysis, the difference between the result obtained from the S2 simulation and the fourth-order Richardson extrapolation leads to an estimate of the discretization error of about 1.5%.

For the `lq1:2` simulations, we have undertaken a separate convergence analysis of `lq1:2-p0086` using the same grid setup as in Table III, but using higher resolutions $h_L/M_1 = 1/24$, $1/28$, and $1/32$. We observe convergence close to fourth order and obtain an error estimate of 1% from the Richardson-extrapolated kick for the medium resolution $h_L/M_1 = 1/28$.

In summary, the LEAN simulations of sequence `sq1:2` are performed with resolution grid S2 of Table III and an

TABLE III. Grid configurations used for LEAN simulations. As explained in Sec. II A 2, the total number of refinement levels is $L + 1$, the number of fixed refinement levels is $l_F + 1$, R_0 is the half-length of the outer grid, R_L is the half-length of one cubic component of the innermost grid, and h_L is the grid spacing on the finest level.

Label	L	l_F	R_0	R_L	h_L/M_1
S1	7	4	384	1	1/20
S2	7	4	384	1	1/24
S3	7	4	384	1	1/32
S4	7	4	384	1	1/28

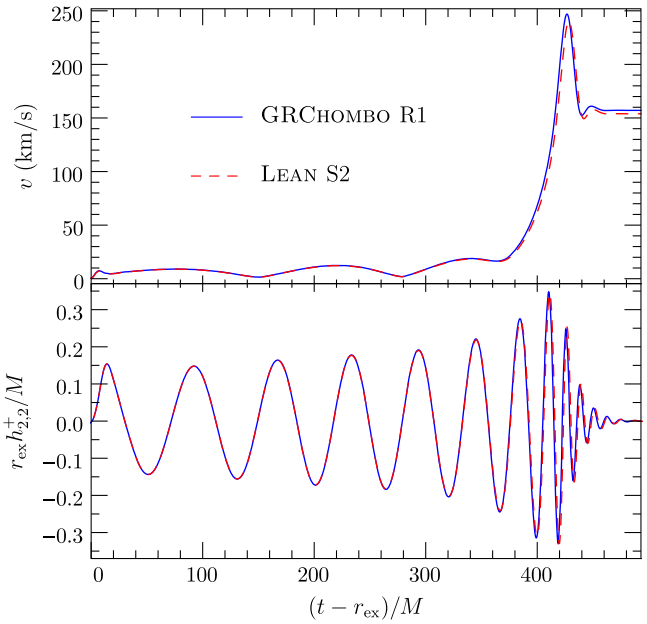

FIG. 7. Comparison between GRChombo and LEAN for the accumulated linear momentum radiated in GWs in simulations of `sq1:2-p0100` with $e_t = 0.10$. We compare the BH recoil velocity (top panel) and the corresponding plus-polarized $\ell = m = 2$ strain amplitude (bottom panel).

error budget of 3.5%, and those of sequence `lq1:2` with grid S4 of Table III and an error budget of 3%.

3. Comparison between GRChombo and LEAN

A comparison of the recoil velocity computed from GRChombo and LEAN simulations of `sq1:2-p0100` with the grid configurations R1 and S2 (used for the `sq2:3` and `sq1:2` runs) respectively, is shown in the top panel of Fig. 7. The eccentricity estimate for this system is $e_t = 0.10$. We have chosen this configuration for two reasons. First, to determine appropriate resolutions, we had to calibrate our codes' accuracy at the start of our exploration, which we began in the regime of mild eccentricities to acquire an intuitive understanding of their behavior. Second, configurations with mild eccentricity have a longer inspiral phase than highly eccentric ones, and therefore impose a stronger requirement on phase accuracy. A mildly eccentric binary is therefore ideally suited to obtain a conservative estimate of the numerical accuracy, which is representative across the targeted parameter space.

The final recoil velocities obtained for this configuration with our two codes differ by about 2%, which is well within the error budget of each code. We also show the quadrupole contribution $h^{+}_{2,2}$ to the + polarization strain defined by [99]

$$h^{+}_{\ell,m}(t,r) - \mathrm{i}h^{\times}_{\ell,m}(t,r) = a_{\ell,m} + b_{\ell,m}t + \int_0^t \mathrm{d}t' \int_0^{t'} \mathrm{d}t'' \psi_{\ell,m}(t'',r), \quad \text{(A1)}$$

where the constants $a_{\ell,m}$ and $b_{\ell,m}$ are chosen to minimize linear drift, in the bottom panel of the figure, to better illustrate the agreement between the codes for these grid configurations.

In Fig. 6 the differences between the results of different resolutions with LEAN are greater than that of GRChombo. However, we found that LEAN entered the convergent regime at lower resolutions than GRChombo. This is compatible with the observations of Ref. [64] that higher resolutions were required for convergence with CCZ4 compared to BSSNOK.

APPENDIX B: GRCHOMBO TAGGING CRITERION

As explained in Sec. II A 1, the regridding is controlled by the tagging of cells for refinement in the Berger-Rigoutsos algorithm [67], with cells being tagged if the tagging criterion C exceeds the specified threshold value t_R as given in Table II. For this work, we use the tagging criterion

$$C = \begin{cases} 0, & \text{if } l \geq l^{\max}_{\mathrm{BH}} \quad \text{and} \quad r_{\mathrm{BH}} < (M_{\mathrm{BH}} + b), \\ \max(C_\chi, C_{\mathrm{punc}}, C_{\mathrm{ex}}), & \text{otherwise,} \end{cases} \quad \text{(B1)}$$

where $l^{\max}_{\mathrm{BH}}$ is a specifiable maximum level parameter for each BH (so that it is not unnecessarily over resolved), r_{BH} is the coordinate distance to the puncture, M_{BH} is the mass of the corresponding BH, b is a buffer parameter, and C_χ, C_{punc}, and C_{ex} are given as follows:

(i) C_χ tags regions in which the gradients of the conformal factor χ become steep. It is given by

$$C_\chi = h_l \sqrt{\sum_{i,j} (\partial_i \partial_j \chi)^2}, \quad \text{(B2)}$$

where h_l is the grid spacing on refinement level l.

(ii) C_{punc} tags within spheres around each puncture in order to ensure the horizon is suitably well resolved. It is given by

$$C_{\mathrm{punc}} = \begin{cases} 100, & \text{if } r_{\mathrm{BH}} < (M_{\mathrm{BH}} + b) 2^{\max(l^{\max}_{\mathrm{BH}} - l - 1, 2)}, \\ 0, & \text{otherwise.} \end{cases} \quad \text{(B3)}$$

(iii) $C_{\rm ex}$ ensures each sphere on which we extract the Weyl scalar Ψ_4 is suitably well resolved. It is given by

$$C_{\rm ex} = \begin{cases} 100, & \text{if } r < 1.2 r_{\rm ex} \quad \text{and} \quad l < l_{\rm ex}, \\ 0, & \text{otherwise}, \end{cases} \tag{B4}$$

where r is the coordinate distance to the center of mass, $r = r_{\rm ex}$ gives the location of the extraction sphere, and $l_{\rm ex}$ is a specifiable extraction level parameter for each sphere.

We also used this tagging criterion with the replacement $r_{\rm BH} \to \max(x_{\rm BH}, y_{\rm BH}, z_{\rm BH})$, where, e.g., $x_{\rm BH}$ is the distance to the puncture in the x direction. We refer to this as "box" tagging and the original as "spherical" tagging. Naively, one might hope that C_χ is sufficient to ensure suitable refinement around the BHs, since the gradients of χ become increasingly steep close to the punctures. However, we found empirically that, without $C_{\rm punc}$, the horizons are perturbed significantly by the refinement boundaries, leading to lower accuracy.

[1] B. P. Abbott *et al.*, Phys. Rev. Lett. **116**, 061102 (2016).
[2] P. R. Saulson, Gen. Relativ. Gravit. **43**, 3289 (2011).
[3] M. Campanelli, C. O. Lousto, and Y. Zlochower, Phys. Rev. D **74**, 041501(R) (2006).
[4] U. Sperhake, V. Cardoso, F. Pretorius, E. Berti, T. Hinderer, and N. Yunes, Phys. Rev. Lett. **103**, 131102 (2009).
[5] W. B. Bonnor, M. A. Rotenberg, Proc. R. Soc. A **265**, 109 (1961).
[6] A. Peres, Phys. Rev. **128**, 2471 (1962).
[7] J. D. Bekenstein, Astrophys. J. **183**, 657 (1973).
[8] D. Gerosa and C. J. Moore, Phys. Rev. Lett. **117**, 011101 (2016).
[9] J. C. Bustillo, J. A. Clark, P. Laguna, and D. Shoemaker, Phys. Rev. Lett. **121**, 191102 (2018).
[10] C. O. Lousto and J. Healy, Phys. Rev. D **100**, 104039 (2019).
[11] V. Varma, M. Isi, and S. Biscoveanu, Phys. Rev. Lett. **124**, 101104 (2020).
[12] V. Cardoso and C. F. B. Macedo, Mon. Not. R. Astron. Soc. **498**, 1963 (2020).
[13] M. J. Fitchett, Mon. Not. R. Astron. Soc. **203**, 1049 (1983).
[14] L. Blanchet, M. S. Qusailah, and C. M. Will, Astrophys. J. **635**, 508 (2005).
[15] S. A. Hughes, M. Favata, and D. E. Holz, in *Conference on Growing Black Holes: Accretion in a Cosmological Context* (Springer, Berlin, Heidelberg) (2004).
[16] T. Damour and A. Gopakumar, Phys. Rev. D **73**, 124006 (2006).
[17] C. F. Sopuerta, N. Yunes, and P. Laguna, Phys. Rev. D **74**, 124010 (2006); **75**, 069903(E) (2007); **78**, 049901(E) (2008).
[18] C. F. Sopuerta, N. Yunes, and P. Laguna, Astrophys. J. Lett. **656**, L9 (2007).
[19] A. Le Tiec, L. Blanchet, and C. M. Will, Classical Quantum Gravity **27**, 012001 (2010).
[20] J. G. Baker, J. Centrella, D.-I. Choi, M. Koppitz, J. R. van Meter, and M. Miller, Astrophys. J. Lett. **653**, L93 (2006).
[21] J. A. Gonzalez, U. Sperhake, B. Bruegmann, M. Hannam, and S. Husa, Phys. Rev. Lett. **98**, 091101 (2007).
[22] F. Herrmann, I. Hinder, D. Shoemaker, and P. Laguna, Classical Quantum Gravity **24**, S33 (2007).
[23] J. A. González, M. D. Hannam, U. Sperhake, B. Brügmann, and S. Husa, Phys. Rev. Lett. **98**, 231101 (2007).
[24] M. Campanelli, C. O. Lousto, Y. Zlochower, and D. Merritt, Phys. Rev. Lett. **98**, 231102 (2007).
[25] M. Campanelli, C. O. Lousto, Y. Zlochower, and D. Merritt, Astrophys. J. Lett. **659**, L5 (2007).
[26] C. O. Lousto and Y. Zlochower, Phys. Rev. Lett. **107**, 231102 (2011).
[27] J. D. Schnittman and A. Buonanno, Astrophys. J. Lett. **662**, L63 (2007).
[28] M. Dotti, M. Volonteri, A. Perego, M. Colpi, M. Ruszkowski, and F. Haardt, Mon. Not. R. Astron. Soc. **402**, 682 (2010).
[29] M. Kesden, U. Sperhake, and E. Berti, Astrophys. J. **715**, 1006 (2010).
[30] C. O. Lousto, Y. Zlochower, M. Dotti, and M. Volonteri, Phys. Rev. D **85**, 084015 (2012).
[31] E. Berti, M. Kesden, and U. Sperhake, Phys. Rev. D **85**, 124049 (2012).
[32] S. Komossa, Adv. Astron. **2012**, 364973 (2012).
[33] M. Colpi, Space Sci. Rev. **183**, 189 (2014).
[34] L. Blecha, D. Sijacki, L. Z. Kelley, P. Torrey, M. Vogelsberger, D. Nelson, V. Springel, G. Snyder, and L. Hernquist, Mon. Not. R. Astron. Soc. **456**, 961 (2016).
[35] L. Barack *et al.*, Classical Quantum Gravity **36**, 143001 (2019).
[36] D. Merritt, M. Milosavljevic, M. Favata, S. A. Hughes, and D. E. Holz, Astrophys. J. Lett. **607**, L9 (2004).
[37] M. J. Benacquista and J. M. Downing, Living Rev. Relativity **16**, 4 (2013).
[38] J. Morawski, M. Giersz, A. Askar, and K. Belczynski, Mon. Not. R. Astron. Soc. **481**, 2168 (2018).
[39] Z. Haiman, Astrophys. J. **613**, 36 (2004).
[40] M. J. Graham, K. E. S. Ford, B. McKernan, N. P. Ross, D. Stern, K. Burdge, M. Coughlin *et al.*, Phys. Rev. Lett. **124**, 251102 (2020).
[41] H.-Y. Chen, C.-J. Haster, S. Vitale, W. M. Farr, and M. Isi, arXiv:2009.14057.
[42] U. Sperhake, R. Rosca-Mead, D. Gerosa, and E. Berti, Phys. Rev. D **101**, 024044 (2020).
[43] J. Samsing and E. Ramirez-Ruiz, Astrophys. J. Lett. **840**, L14 (2017).
[44] J. Samsing, Phys. Rev. D **97**, 103014 (2018).
[45] J. Samsing, A. Askar, and M. Giersz, Astrophys. J. **855**, 124 (2018).

[46] C. L. Rodriguez, P. Amaro-Seoane, S. Chatterjee, K. Kremer, F. A. Rasio, J. Samsing, C. S. Ye, and M. Zevin, Phys. Rev. D **98**, 123005 (2018).
[47] J. Samsing, I. Bartos, D. D'Orazio, Z. Haiman, B. Kocsis, N. Leigh, B. Liu, M. Pessah, and H. Tagawa, arXiv:2010.09765.
[48] H. Tagawa, B. Kocsis, Z. Haiman, I. Bartos, K. Omukai, and J. Samsing, Astrophys. J. Lett. **907**, L20 (2021).
[49] V. Cardoso, C. F. B. Macedo, and R. Vicente, Phys. Rev. D **103**, 023015 (2020).
[50] B. P. Abbott *et al.* (LIGO Scientific and Virgo Collaborations), Astrophys. J. **883**, 149 (2019).
[51] R. Abbott *et al.* (LIGO Scientific and Virgo Collaborations), Phys. Rev. Lett. **125**, 101102 (2020).
[52] I. M. Romero-Shaw, P. D. Lasky, E. Thrane, and J. C. Bustillo, Astrophys. J. Lett. **903**, L5 (2020).
[53] V. Gayathri, J. Healy, J. Lange, B. O'Brien, M. Szczepanczyk, I. Bartos, M. Campanelli, S. Klimenko, C. Lousto, and R. O'Shaughnessy, arXiv:2009.05461.
[54] A. Nishizawa, E. Berti, A. Klein, and A. Sesana, Phys. Rev. D **94**, 064020 (2016).
[55] K. Breivik, C. L. Rodriguez, S. L. Larson, V. Kalogera, and F. A. Rasio, Astrophys. J. Lett. **830**, L18 (2016).
[56] A. Nishizawa, A. Sesana, E. Berti, and A. Klein, Mon. Not. R. Astron. Soc. **465**, 4375 (2017).
[57] C. Roedig and A. Sesana, J. Phys. Conf. Ser. **363**, 012035 (2012).
[58] M. Bonetti, A. Sesana, F. Haardt, E. Barausse, and M. Colpi, Mon. Not. R. Astron. Soc. **486**, 4044 (2019).
[59] E. Huerta *et al.*, Phys. Rev. D **100**, 064003 (2019).
[60] K. Clough, P. Figueras, H. Finkel, M. Kunesch, E. A. Lim, and S. Tunyasuvunakool, Classical Quantum Gravity **32**, 245011 (2015).
[61] http://www.grchombo.org/.
[62] U. Sperhake, Phys. Rev. D **76**, 104015 (2007).
[63] S. Husa, J. A. Gonzalez, M. Hannam, B. Bruegmann, and U. Sperhake, Classical Quantum Gravity **25**, 105006 (2008).
[64] D. Alic, C. Bona-Casas, C. Bona, L. Rezzolla, and C. Palenzuela, Phys. Rev. D **85**, 064040 (2012).
[65] D. Alic, W. Kastaun, and L. Rezzolla, Phys. Rev. D **88**, 064049 (2013).
[66] M. Adams *et al.*, Lawrence Berkeley National Laboratory Tech. Report No. LBNL-6616E, 2019.
[67] M. Berger and I. Rigoutsos, IEEE Trans. Sysr. Man Cybernet. **21**, 1278 (1991).
[68] T. Goodale, G. Allen, G. Lanfermann, J. Massó, T. Radke, E. Seidel, and J. Shalf, in *Vector and Parallel Processing—VECPAR'2002, 5th International Conference, Lecture Notes in Computer Science* (Springer, Berlin, 2003).
[69] T. Nakamura, K. Oohara, and Y. Kojima, Prog. Theor. Phys. Suppl. **90**, 1 (1987).
[70] M. Shibata and T. Nakamura, Phys. Rev. D **52**, 5428 (1995).
[71] T. W. Baumgarte and S. L. Shapiro, Phys. Rev. D **59**, 024007 (1998).
[72] M. Campanelli, C. Lousto, P. Marronetti, and Y. Zlochower, Phys. Rev. Lett. **96**, 111101 (2006).
[73] J. G. Baker, J. Centrella, D.-I. Choi, M. Koppitz, and J. van Meter, Phys. Rev. Lett. **96**, 111102 (2006).
[74] E. Schnetter, S. H. Hawley, and I. Hawke, Classical Quantum Gravity **21**, 1465 (2004).
[75] J. Thornburg, Phys. Rev. D **54**, 4899 (1996).
[76] J. Thornburg, Classical Quantum Gravity **21**, 743 (2004).
[77] S. Brandt and B. Bruegmann, Phys. Rev. Lett. **78**, 3606 (1997).
[78] J. M. Bowen and J. W. York, Phys. Rev. D **21**, 2047 (1980).
[79] M. Ansorg, B. Bruegmann, and W. Tichy, Phys. Rev. D **70**, 064011 (2004).
[80] V. Paschalidis, Z. B. Etienne, R. Gold, and S. L. Shapiro, arXiv:1304.0457.
[81] U. Sperhake, E. Berti, V. Cardoso, J. A. Gonzalez, B. Bruegmann, and M. Ansorg, Phys. Rev. D **78**, 064069 (2008).
[82] R. Arnowitt, S. Deser, and C. W. Misner, in *Gravitation an Introduction to Current Research*, edited by L. Witten (John Wiley, New York, 1962), pp. 227–265.
[83] B. Bruegmann, J. A. Gonzalez, M. Hannam, S. Husa, U. Sperhake, and W. Tichy, Phys. Rev. D **77**, 024027 (2008).
[84] J. W. York, Jr., *Initial Data for Collisions of Black Holes and Other Gravitational Miscellany* (Cambridge University Press, Cambridge, England, 1989), p. 89.
[85] N. Loutrel, S. Liebersbach, N. Yunes, and N. Cornish, Classical Quantum Gravity **36**, 025004 (2019).
[86] R.-M. Memmesheimer, A. Gopakumar, and G. Schaefer, Phys. Rev. D **70**, 104011 (2004).
[87] M. Campanelli and C. O. Lousto, Phys. Rev. D **59**, 124022 (1999).
[88] C. O. Lousto and Y. Zlochower, Phys. Rev. D **76**, 041502(R) (2007).
[89] M. Ruiz, R. Takahashi, M. Alcubierre, and D. Nunez, Gen. Relativ. Gravit. **40**, 2467 (2008).
[90] J. Healy, C. O. Lousto, and Y. Zlochower, Phys. Rev. D **96**, 024031 (2017).
[91] B. Brügmann, J. A. González, M. D. Hannam, S. Husa, and U. Sperhake, Phys. Rev. D **77**, 124047 (2008).
[92] C. O. Lousto, H. Nakano, Y. Zlochower, and M. Campanelli, Phys. Rev. D **81**, 084023 (2010); **82**, 129902(E) (2010).
[93] A. G. Wiseman, Phys. Rev. D **46**, 1517 (1992).
[94] M. Kesden, D. Gerosa, R. O'Shaughnessy, E. Berti, and U. Sperhake, Phys. Rev. Lett. **114**, 081103 (2015).
[95] D. Gerosa, M. Kesden, U. Sperhake, E. Berti, and R. O'Shaughnessy, Phys. Rev. D **92**, 064016 (2015).
[96] C. Hamilton and R. R. Rafikov, Mon. Not. R. Astron. Soc. **488**, 5489 (2019).
[97] C. Hamilton and R. R. Rafikov, Mon. Not. R. Astron. Soc. **488**, 5512 (2019).
[98] U. Sperhake, B. Bruegmann, D. Muller, and C. Sopuerta, Classical Quantum Gravity **28**, 134004 (2011).
[99] N. T. Bishop and L. Rezzolla, Living Rev. Relativity **19**, 2 (2016).